The Astrophysical Journal, 923:107 (8pp), 2021 December 10 https://doi.org/10.3847/1538-4357/ac2eb7

Spatial Variation in Temperature and Density in the IC 63 PDR from H_2 Spectroscopy

Archana Soam[1], B-G Andersson[1], Janik Karoly[1,2], Curtis DeWitt[1], and Matthew Richter[3]
[1] SOFIA Science Center, Universities Space Research Association, NASA Ames Research Center, M.S. N232-12, Moffett Field, CA 94035, USA; asoam@usra.edu
[2] Jeremiah Horrocks Institute, University of Central Lancashire, Preston PR1 2HE, UK
[3] Department of Physics and Astronomy, University of California, Davis, CA, USA
Received 2021 July 13; revised 2021 October 8; accepted 2021 October 9; published 2021 December 15

Abstract

We have measured the gas temperature in the IC 63 photodissociation region (PDR) using the S(1) and S(5) pure rotation lines of molecular hydrogen with SOFIA/EXES. We divide the PDR into three regions for analysis based on the illumination from γ Cas: sunny, ridge, and shady. Constructing rotation diagrams for the different regions, we obtain temperatures of $T_{ex} = 562^{+52}_{-43}$ K toward the ridge and $T_{ex} = 495^{+28}_{-25}$ K in the shady side. The H_2 emission was not detected on the sunny side of the ridge, likely due to the photodissociation of H_2 in this gas. Our temperature values are lower than the value of $T_{ex} = 685 \pm 68$ K using the S(1), S(3), and S(5) pure rotation lines, derived by Thi et al. using lower spatial resolution ISO-SWS data at a different location of the IC 63 PDR. This difference indicates that the PDR is inhomogeneous and illustrates the need for high-resolution mapping of such regions to fully understand their physics. The detection of a temperature gradient correlated with the extinction into the cloud, points to the ability of using H_2 pure rotational line spectroscopy to map the gas temperature on small scales. We used a PDR model to estimate the FUV radiation and corresponding gas densities in IC 63. Our results shows the capability of SOFIA/EXES to resolve and provide detailed information on the temperature in such regions.

Unified Astronomy Thesaurus concepts: Photodissociation regions (1223); Interstellar molecules (849)

1. Introduction

Molecular hydrogen is readily detectable in photodissociation regions (PDRs; Nadeau et al. 1991; Timmermann et al. 1996; van Dishoeck 2004). Hydrogen transitions from H_2, via H I to H II in PDRs from the exposure to far-ultraviolet (FUV) radiation from O/B stars and the interstellar radiation field. Through photochemical reactions and photoelectric emission, both the chemistry and temperature balance of the PDRs is controlled by the FUV radiation (Röllig et al. 2007). It is therefore important to characterize the overall as well as small-scale structure of these regions.

In the regions directly affected by FUV radiation, the thermal balance is related to the radiative transfer of the UV photons. The FUV radiation is also responsible for the kinematics and chemical changes of these regions (Draine & Bertoldi 1999). The ejection of photoelectrons from the dust grains is the process accountable for heating of the region (Bakes & Tielens 1994; Weingartner & Draine 2001). In addition to this process, the collisional de-excitation of H_2 molecules initially excited by UV photons is also a mechanism contributing to the heating (Sternberg & Dalgarno 1989). Toward the higher density regimes, gas–grain collisions may also heat the gas. On the other hand, the fine-structure lines of neutral atoms or of singly ionized species provide the cooling of the outer layers and CO rotational lines cool the predominantly molecular inner regions (Allers et al. 2005).

The observations of rotational and vibrational lines of molecular hydrogen is a useful tool to diagnose the physical properties of the PDRs. As investigated by Allers et al. (2005) toward Orion bar, the low critical density of the ground-state rotational transitions makes ratios of mid-IR lines good probes of the temperature in the layers where they arise. In PDRs with $n(H) \sim 10^4$–10^5 cm^{-3}, the lower rotational levels of H_2 (i.e., $J = 2$–0, $J = 3$–1) are maintained in thermal equilibrium by collisions (Habart et al. 2005). The critical density of $n(H) > 10^5$ cm^{-3} is needed for higher transitions (i.e., $J = 5$–3, $J = 7$–5). The populations of these levels can be a good tracer of gas temperature.

We investigated the pure rotational molecular hydrogen line emission in the PDR IC 63. This is a small, but well-studied (at $d \approx 200$ pc; Karr et al. 2005), PDR irradiated by the (FUV) light from γ Cas, a B0.5 IV type star located ~1.3 pc projected distance from the cloud. This is the nearest well-explored H II system to investigate the PDR properties. The system contains nebaule IC 59 and IC 63 irradiated by γ Cas. The projected direction of FUV radiation from γ Cas on IC 63 is from southwest to northeast.

The goal of SOFIA proposal 07_0040 (PI: Soam, A.) was to quantify the difference in gas temperature in gas directly exposed to the light from γ Cas, and gas in the shade of a molecular clump within the PDR. Here, we present results of observations of the S(1) and S(5) lines of H_2. We compare our Stratospheric Observatory for Infrared Astronomy (SOFIA) Echelon-Cross-Echelle Spectrograph (EXES; Richter et al. 2018) findings with the results of Thi et al. (2009) toward a different location of the IC 63 PDR. As is often the case in the ISM (Ehrenfreund et al. 1998), Thi et al. (2009), using observations of S(0), S(1), S(3), and S(5) from the Short Wavelength Spectrometer (SWS) on board the Infrared Space Observatory (ISO), found a two-temperature structure in the H_2 excitation. The two lowest rotation transitions found a low temperature, typical of the cold neutral medium (McKee & Ostriker 1977), in their case $T_{ex} = 106 \pm 11$ K, while their three highest transitions yield a significantly higher temperature of $T_{ex} = 685 \pm 68$ K.

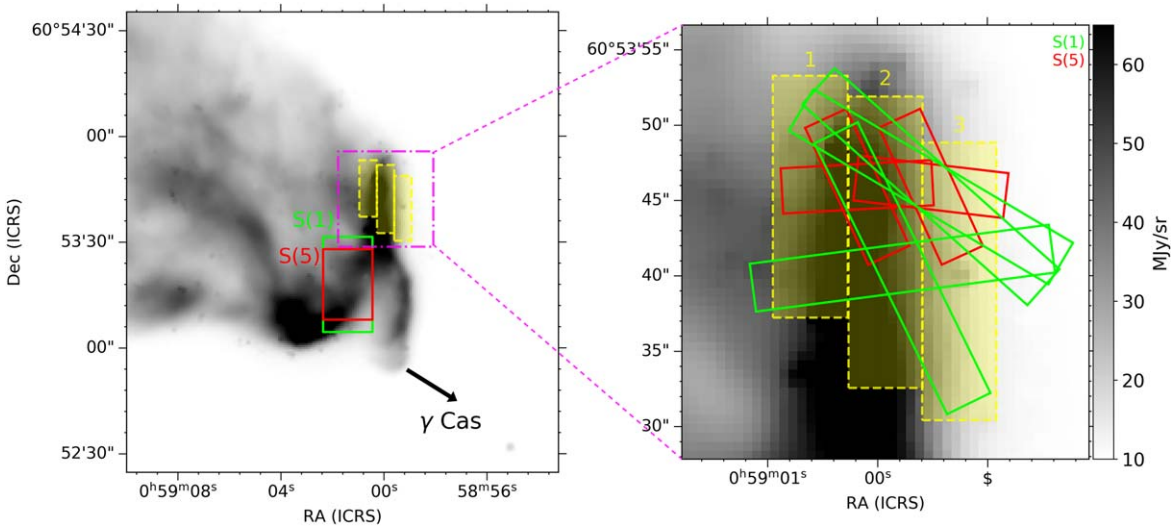

Figure 1. Left panel shows the location of the ISO/SWS slits and the three EXES regions over an 8.0 μm Spitzer IRAC image (taken from Spitzer archive). The larger solid green rectangle is the ISO/SWS S(1) (17.0μm) aperture and the red solid rectangle is the S(5) (6.9 μm) aperture (Thi et al. 2009). The purple dotted–dashed line shows the zoomed-in image in the right panel and the yellow rectangles show the three regions observed by SOFIA/EXES. The direction to γ Cas is shown as well. The right panel shows the zoomed-in view of the three extraction regions and the EXES slit positions over the 8.0 μm IRAC image. The SOFIA/EXES S(1) aperture is the larger solid green rectangles and the S(5) aperture is the smaller solid red rectangles. The slits swept clockwise during observations. We have defined region 1 as shady, region 2 as ridge, and region 3 as sunny and they are shown as translucent yellow rectangles.

Such high(er) excitation temperatures in the high J lines of H_2 are commonly seen in FUV absorption spectroscopy and have been variously attributed to the effects of UV pumping via the Lyman and Werner band excitations (e.g., Jura 1975) and to collisional heating, including through shocks.

Andrews et al. (2018) investigated the physical conditions of UV-illuminated surface of IC 63. Using archival Spitzer IRS data of molecular hydrogen in IC 63, they constructed the excitation diagram to find gas temperature in IC 63 PDR. Assuming that lines are optically thin, adopting an ortho-to-para ratio of three, and using energies and Einstein coefficients from Rosenthal et al. (2000), they found two-temperature components in IC 63 PDR.

The observed correlation between the column densities of the CH^+ ion (whose formation, via the reaction of C^+ with H_2, includes a ~4600 K activation barrier; Millar et al. 1991) and H_2 $J = 3$ and $J = 5$ (e.g., Lambert & Danks 1986) indicates that collisional excitation does contribute to the high-J population of H_2.

In PDRs, FUV pumping, photodissociation, and photoelectric emission are critical processes. On the PDR outer boundary, hydrogen exists mainly in atomic form because most of the molecular hydrogen is photodissociated by the high energy UV photons (Thi et al. 2009). As we move into, or behind, high density/extinction regions inside the PDR, the strength of the UV radiation is reduced by dust extinction, which, together with line self-shielding, reduces the photodissociation in comparison to H_2 formation on the dust grain surface and the molecular fraction increases (Habart et al. 2004, 2011). While the cutoff for photoelectric heating is not at quite as short a wavelength as for H_2 destruction (1550 Å for an assumed work function of 8 eV; Weingartner et al. 2006), the extinction at such wavelengths is still very steep. As the shielding increases, we would therefore expect the gas temperature to drop. In an inhomogeneous medium where significant shading occurs due to opaque clumps, a (variable) two-temperature structure would be expected, corresponding to gas experiencing limited or significant FUV extinction. Given the size and location of the Thi et al. (2009) ISO apertures (i.e., ≈25″ or 0.025 pc at the distance of IC 63), it is conceivable that their two-temperature result originate from a mixture of gas at the front and back of the H → H_2 transition over their apertures (Figure 1). Therefore, we set out to investigate the variation of the temperatures (if present) throughout the PDR, using higher spatial resolution observations than those from ISO/SWS. With its narrow slit, EXES on SOFIA has the capability to produce such higher spectral resolution data for these investigations.

The goal of this paper is to investigate gas temperatures in those regions of IC 63 PDR that are directly illuminated by and in the shade of UV radiation from γ Cas. Section 2 presents the details of SOFIA/EXES observations. Section 3 presents our results and analysis performed. Section 4 shows the detailed discussion of our results and Section 5 concludes our findings.

2. Observations

2.1. Pure Rotational Lines

We observed IC 63 with SOFIA using the EXES instrument in its high-medium mode (Richter et al. 2018), selecting the highest operable cross dispersion order to maximize the spatial length of the slit. For the H_2 S(1) observations, we observed at 587 cm^{-1} in third order, with a slit length of 19″ (0.0184 pc assuming a distance of ≈200 pc). For H_2 S(5), we observed at 1447 cm^{-1} in eighth order, with a slit length of 10″ (0.0097 pc). All observations used the 3.″2 (0.0031 pc) slit width, which provides $R \sim 60{,}000$ resolution, or ~5 km s^{-1} (measured with laboratory gas cell data prior to flight (EXES PI team, 2021, private communication)).

We observed IC 63 using off-source nodding. We selected an off-region of blank sky 30″ east of the central slit coordinate (Table 1) and nodded at intervals of 60 s in order to subtract telluric emission and thermal background from the on-source integration.

The spatial resolution of the observations is approximately 3.″7 for both wavelengths, which is taken from the 50%

Table 1
Details of SOFIA/EXES Observations of IC 63

UT DATE	Line Transition	$\lambda_{central}$ (μm)	Central Coordinate (R.A.$_{J2000}$, Decl.$_{J2000}$)	VPA[a] Range (°)	Doppler Offset (km s^{-1})	Int. Time (s)
2018-10-19	S(1) 3–1	17.03	00:58:59.8600, +60:53:39.900	97.4377-26.1064	−12.14	2704
2018-10-20	S(5) 7–5	6.91	00:59:00.2700, +60:53:45.300	93.1134-24.7629	−11.81	5532
2018-10-24	S(5) 7–5	6.91	00:58:59.6000, +60:53:45.300	83.2769-24.613	−10.52	4992
2018-10-25	S(1) 3–1	17.03	00:58:59.6000, +60:53:45.300	59.3702-48.2404	−10.17	896

Note.
[a] Vertical position angle (VPA), defined as degrees east of north.

encircled energies reported in the SOFIA observatory characterization (Temi et al. 2018). The telescope was guided using the Focal Plane Imager Plus (FPI+) guider camera on a visually bright star offset from IC 63. This mode of guiding is astrometrically accurate to 0.″41 with each new target acquisition and with a median pointing stability of 0.″17 following acquisition (Temi et al. 2018).

Flux calibration was done by scaling the data to spectral flat fields with the instrument's external blackbody source before each observation. The resulting absolute flux calibration is good to 25%. The relative flux calibration between S(1) and S(5) is 12.5% but any systematic differences in the relative or the absolute flux calibration are repeatable to 2% (EXES PI team, private communication).

The rotation of field for SOFIA observations is determined by the heading of the airplane but can be held fixed for short periods by the telescope. Because EXES does not have a field rotator, as some other SOFIA instruments, the slit position angle (PA) changed by discrete amounts every 6 minutes during the observations. We executed individual nodded files within that interval, typically obtaining 4 nod pairs per file and per discrete PA. Table 1 reports the starting and ending slit position angles, which are also visualized in Figure 1.

Data were reduced using with the SOFIA Redux pipeline (Clarke et al. 2015), including steps for spike removal, nod-subtraction, flat-fielding, flux calibration, order rectification, and coadding of nodded pairs. The wavelength scales were calibrated by matching the sky emission lines within the spectral settings to their values in the HITRAN database (Gordon et al. 2017). The uncertainty in the wavelength solution is estimated to be $\sim$0.3 km s^{-1}.

Because of the changing slit angle during observations, we employed a customized procedure for combining the data. We defined three 5″-width intervals of R.A., as shown in Figure 1. The R.A. centers of the regions were (1) 00:59:00.61, (2) 00:58:59.93, and (3) 00:58:59.25. We used the central slit coordinate and position angle of each file to assign and extract the appropriate parts of the 2D spectrum to regions 1–3, weighting each extracted spatial row by the file's integration time. Because there were up to 20 nodded files and different position angles used during each night's observation, we only list the starting and ending position angle in Table 1.

Our observations of the H_2 S(1) and S(5) lines with the narrower EXES slit toward IC 63 are located in a region chosen to provide as narrow a PDR ridge as possible, somewhat north of the region observed by Thi et al. (2009). The location of the EXES slits and the Thi et al. (2009) apertures are shown on Spitzer IRAC image of IC 63 in Figure 1. In the left panel of Figure 1, the green and red rectangles show the locations of the ISO/SWS slits for S(1) and S(5) observations of Thi et al. (2009) while the observed regions by EXES are shown with semitransparent yellow rectangles. We designated these regions, labeled as 1, 2, and 3 in the right panel of Figure 1, as the shady, ridge, and sunny sides, respectively, of the PDR. The right panel of Figure 1 also shows the EXES slit rotation pattern and actual extraction regions of S(1) and S(5) emission shown with green and red rectangles, respectively.

The simple vertical R.A. bars we used for regions were well-motivated by the 2.12 μm rovibrational H_2 emission and 8.0 μm Spitzer/IRAC emission (Figure 1). Because of the exploratory nature of the observations, most of the S(1) was acquired in regions that were close but did not strictly overlap the S(5) coverage. But the full integration time/spatial extent of the S(1) line was needed to obtain a useful line detection. This might mean that the temperature gradient reported here could be mimicked by an inopportune brightness gradient between the total S(1) footprint and the S(5) footprint. However, the 2.12 μm rovibrational emission and Spitzer/IRAC image do not suggest such a gradient.

2.2. Near-infrared Imaging of Rovibrational Line

We also adopted H_2 1−0 S(1) line observations of IC 63 at 2.122 μm from Andersson et al. (2013) for our analysis in this work. They acquired this data from the WIRCam instrument (Puget et al. 2004) at the Canada–France–Hawaii Telescope (CFHT) in queue observing mode during 2008 August 12–September 14. In these observations, Andersson et al. (2013) used *Ks* filter to estimate the continuum contributions to the nebular emission because the narrowband continuum filter associated with the H_2 10 S(1) filter was not installed at the time of these observations. The data was reduced using the observatory pipeline. The photometric calibration of the data was achieved using several hundred 2MASS (Skrutskie et al. 2006) stars in the observed field. More details of observations, data reduction, and calibration can be seen in the paper by Andersson et al. (2013).

3. Results and Analysis

Figure 2 shows the spectra for the S(1) and S(5) lines. We measured flux values for the S(1) and S(5) lines in the ridge and shady regions, but we detected no emission in the sunny region (Table 2). We calculated the flux values shown in Table 2 by calculating the area of the Gaussian fits of the line spectra shown in Figure 2. The line widths used to calculate these areas are shown in Table 2. We compared this with the direct line integration method and found agreeing flux values. The flux uncertainties are derived from the uncertainties of the fitted Gaussian parameters. The integrated intensity of the S(1) line in the shady region is a factor of 2 larger than that in the ridge

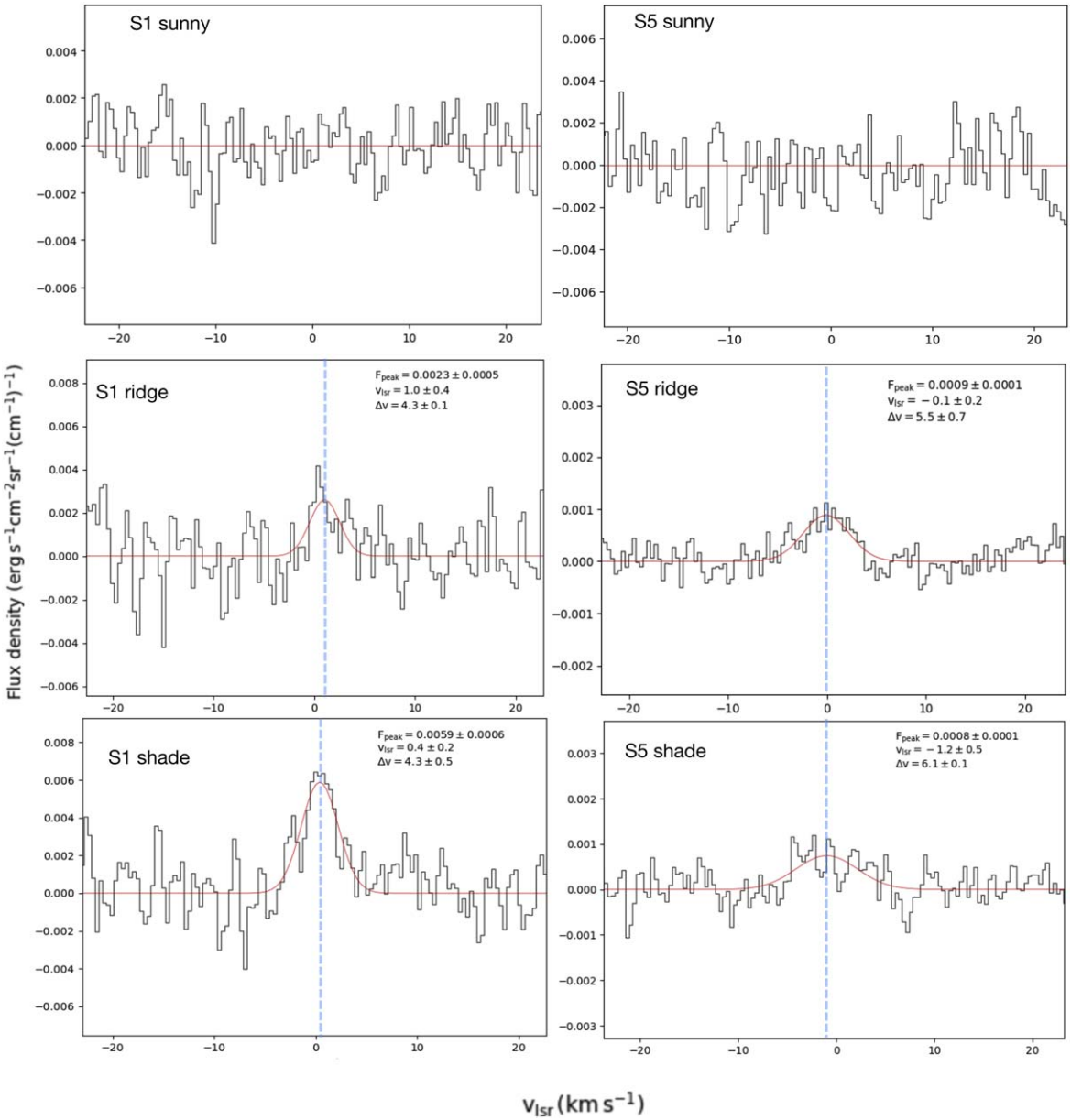

Figure 2. The line profiles of S(1) and S(5) H_2 emissions in ridge and shady sides of IC 63 PDR. No emission is detected in the sunny side of the PDR. The dashed blue line shows the center of the detected emission and the red solid line shows the Gaussian fit of the emission.

region, which indicates warmer gas in the ridge region. The integrated intensity of the S(5) line is approximately the same in both regions. The S(1) integrated intensity in the ridge region agrees with the S(1) ISO SWS intensity from Thi et al. (2009) while the ISO SWS S(5) value is approximately twice the intensity of the EXES S(5) intensity values in both regions.

3.1. Rotation Diagram

We calculated the population of the upper level, N_u, using the equation:

$$I_{ul} = N_u A_{ul} h\nu_{ul}/4\pi, \quad (1)$$

where I_{ul} is the total intensity, A_{ul} is the Einstein A-coefficient, and ν_{ul} is the frequency of the transitions from the upper to lower levels. We constructed an H_2 excitation diagram (see Figure 3) by plotting the log of the population of the upper level divided by the upper level degeneracy and nuclear spin degeneracy (g_u, g_I respectively) versus the temperatures of the upper energy levels, which are 1015 K for S(1) and 4586 K for S(5). The excitation temperature at local thermodynamic equilibrium, T_{ex}, can be related to the population of the upper level, N_u, by the equation:

$$N_u = N(H_2) g_I g_u e^{-E_{ul}/T_{ex}}/Q(T_{ex}), \quad (2)$$

where E_{ul} is the energy of the transition expressed in Kelvin, $N(H_2)$ is the H_2 column density, and $Q(T_{ex})$ is the partition function. In the rotational excitation diagram shown in Figure 3, we overplotted EXES data (red solid circles) with the data taken from Thi et al. (2009; black filled squares).

Based on these two lines, we derive excitation temperatures of $T_{ridge} = 562^{+52}_{-43}$ K and $T_{shade} = 495^{+28}_{-25}$ K. The errors given here are 1σ level. This shows that the ridge of IC 63 seen with EXES observations is at a similar temperature (within

Table 2
Properties of Observed H_2 Transitions in IC 63 PDR

Line	Reg[a]	λ (μm)	I_{ul} 10^{-5} erg cm^{-2} s^{-1} sr^{-1}	E_{up}/k_B (K)	A_{ul}[b] (s^{-1})	Δv[c] (km s^{-1})
S(1) 3–1	Shady	17.035	5.3 ± 0.8	1015.12	4.8×10^{-10}	4.3 ± 0.5
S(1) 3–1	Ridge	17.035	2.2 ± 0.8	1015.12	4.8×10^{-10}	5.1 ± 1.5
S(1) 3–1	Sunny	17.035	...	1015.12	4.8×10^{-10}	...
S(5) 7–5	Shady	6.901	2.5 ± 0.6	4586.30	5.9×10^{-8}	6.1 ± 1.2
S(5) 7–5	Ridge	6.901	2.6 ± 0.4	4586.30	5.9×10^{-8}	5.5 ± 0.7
S(5) 7–5	Sunny	6.901	...	4586.30	5.9×10^{-8}	...

Notes.
[a] See Figure 1 for explanation of regions.
[b] Einstein *A*-coefficients from Wolniewicz et al. (1998).
[c] Line width values were calculated from inspection of each line profile individually and may differ from values given by the fits in Figure 2.

uncertainties) as the high temperature reported by Thi et al. (2009; $T_{ex} = 685 \pm 68$ K). However, our results show that the shady region of IC 63 is somewhat cooler than their reported temperature. The inferred H_2 column density from the excitation temperatures of the ridge and shady regions are 9.8×10^{19} cm^{-2} and 3.6×10^{20} cm^{-2}, respectively. We could not derive excitation temperature in the sunny side of the cloud as we did not detect either the S(1) or S(5) lines there (see Figure 2).

As shown in the left panel of Figure 1, the SWS footprint is significantly larger than the EXES slit width and located further south—and therefore closer to the illuminating star γ Cas. Because of the area of the SWS aperture, it encompasses gas both on the near and far sides of the fluorescent ridge—as seen from γ Cas. Based on the location and size differences we hypothesize that the warm gas probed by the ISO/SWS measurement may possibly represent higher illumination regions, or a more sunny location and that the EXES observation probe gas with a higher extinction toward the star or a more shady spot if the actual distance of the ISO slit is lesser than that of EXES slit from γ Cas. However, the projected distances from γ Cas of the ISO and EXES slits are almost the same. The cold temperature ($T_{ex} = 106 \pm 11$ K) seen in the ISO data would then be tracing well-shielded gas behind a dense clump. This hypothesis can be tested by extending the wavelength and spatial coverage to probe both the H_2 S(1)/S(0) temperature in the EXES location and by isolating more spatial locations on either side of the PDR ridge. We are currently pursuing such observations.

3.2. PDR Modeling

We used the PDR toolbox (Kaufman et al. 2006; Pound & Wolfire 2008) to model our observed line ratio H_2 1−0 S(1)/0−0 S(1). This model takes into account both thermal and UV excitation for the H_2 level population. We have plotted the predicted values for different values of FUV radiation field intensity (G_0) and volume density (n) in Figure 4, where we have also overplotted the observed line ratios. The upper panel of Figure 4 shows the observed values overplotted for the ridge and shady sides using red and black lines, respectively. The shaded regions show 3σ uncertainties limits in the mean values. We find values of G_0, in shade and ridge of ∼200 and ∼400 in Habing units, respectively. Using conversion from Habing units to Draine units (Draine = 1.7 × Habing; Wolfire & Kaufman 2011), these values are 340 and 680 Draine units in shade and ridge, respectively. The value of G_0 in ridge is consistent to the G_0 value of 650 Draine units reported by Jansen et al. (1994) in IC 63.

The dashed box labeled as 1 in the upper panel of Figure 4 clearly show different G_0 values for the ridge and shady sides (red and black solid lines). This region is zoomed-in in the lower panel of he figure where the G_0 gap is indicated by double headed arrows. We used this difference in G_0 to estimate the gas density in the PDR by adapting the radiative transfer equation:

$$G_{0\text{shade}} = e^{-\tau} G_{0\text{ridge}} \quad (3)$$

where $G_{0\text{shade}}$ and $G_{0\text{ridge}}$ are the model returned values of G_0 for the line ratios observed in the shady and ridge sides of IC 63 PDR, respectively. τ is optical depth of the region for the wavelength determining the line ratio (i.e., gas temperature). Using G_0 values in Equation (3), we estimated an optical depth of 0.4.

In PDRs, when FUV photons are absorbed, the grain may be ionized (photoelectric effect) and part of the photon energy is carried away by the electron, heating the gas. Assuming a work function of 8 eV (Weingartner & Jordan 2008) corresponds to a wavelength of ∼1550 Å we can estimated the gas density in the PDR using the optical depth estimated above. Using relation $A_{1550\,\text{Å}}/A_v = 2.64$ from Whittet (2003), and $A_{1550\,\text{Å}} = 1.086 \times \tau$, we estimated A_v of ∼0.16. This value of A_v and total-to-selective extinction ($R_v = 3.1$) together with the relationship $N(\text{H}) = 1.87 \times 10^{21} A_v$ and $N(\text{H}_2) = 0.5\ N(\text{H})$ from Bohlin et al. (1978), yields a column density $N(\text{H}_2)$ of 2.9×10^{20} cm^{-2}. Assuming a constant space density and that the absorption takes place over a region of projected length L we can estimate the space density. If we assume L to be the EXES slit size of the H_2 S(1) observations i.e., 19″ shown in Figure 1, we estimate a volume density $n(\text{H}_2)$ of 5×10^3 cm^{-3}.

We also estimated column densities in shady (3.6×10^{20} cm^{-2}) and ridge (9.8×10^{19} cm^{-2}) regions of IC 63 from the rotation diagram (Section 3.1). Using these values over a projected length L at the location of EXES slit, we derived space densities of 6.2×10^3 cm^{-3} and 1.7×10^3 cm^{-3} in shady and ridge sides, respectively. These density values are consistent with our findings when assuming heating due to the photoelectric effect. Jansen et al. (1994) presented far-infrared spectroscopic measurements of IC 63. They measured line ratios of CO, HCO^+, HCN, CS and HCHO suggesting that cloud is warm with a temperature ≈50 K, and the density of the gas is 5×10^4 cm^{-3}. This value is ten times higher than our estimation above. It might be possible that the

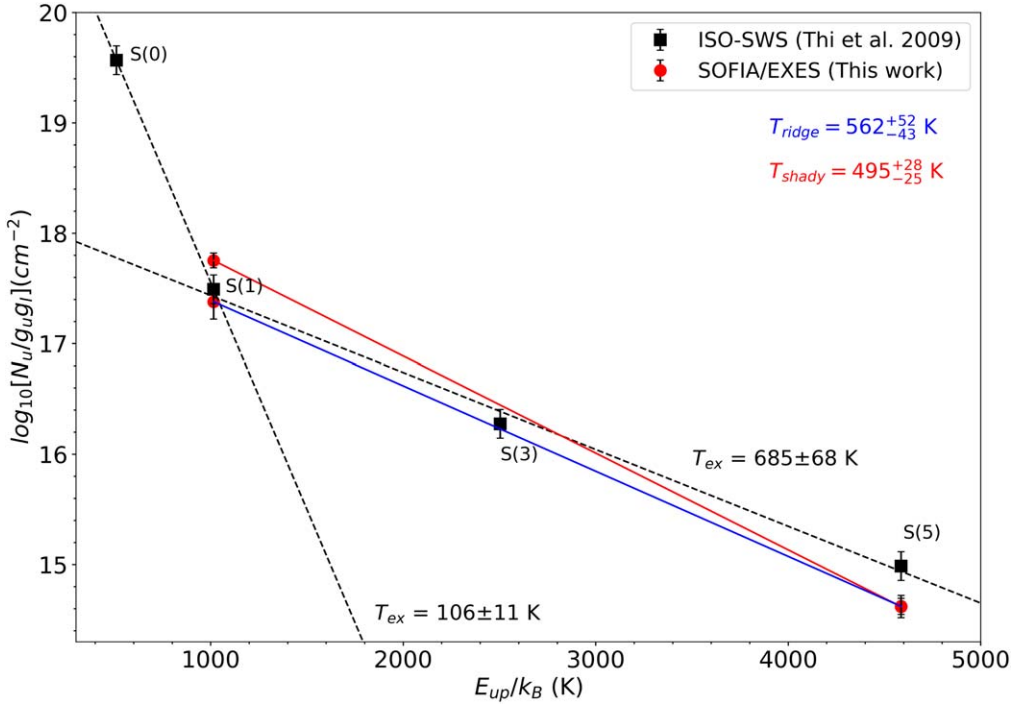

Figure 3. Rotational diagram created with ISO-SWS (solid black rectangles) and EXES data (solid red circles). The two temperatures seen by ISO/SWS data (Thi et al. 2009) are labeled and the temperatures of ridge and shady regions estimated with EXES data also shown with the text in red and blue colors.

values reported in Jansen et al. (1994) are biased toward denser clumps.

As can be noticed in Figure 4, the modeled H_2 1−0 S(1)/0 −0 S(1) line ratio gives a completely different answer for the density. The density value obtained here is of the order of 2×10^2 cm^{-3}. It is also noticed by Thi et al. (2009) that the H_2 S(3)/S(1) line ratio gives a completely different answer for FUV radiation strength and density. Thi et al. (2009) uses the explanation given by Bertoldi (1997) and Allers et al. (2005) to counter these discrepancies. It is suggested that either the H_2 formation rate on grains needs to be larger or the photoelectric heating efficiency needs to be increased at high temperatures, shifting the transition zone of H → H_2 closer to the warm edge of PDRs. High photoelectric heating efficiencies have been calculated by Weingartner & Draine (1999) based on an enhanced dust-to-gas ratio in the PDR due to gas–grain drift. We agree with the findings and possible causes explained by Thi et al. (2009). The photoelectric heating might be underestimated at hotter regions, which may cause discrepancies in the density estimation. Also, we did not include a detailed analysis of H_2 formation rate in this work because that is beyond the purpose of this paper. An underestimation in assuming the rate might also cause the discrepancies between model and observed densities.

4. Discussion

Our results show that SOFIA/EXES is capable of investigating the spatial variation in temperatures in such regions. Although we do not see a big difference from temperature values of Thi et al. (2009), we are capable of better resolving the spatial locations in the IC 63 PDR. The spatial coverage of ISO data used by Thi et al. (2009) was ≈25″ or 0.025 pc at the distance of IC 63.

Andrews et al. (2018) investigated the physical conditions of the UV-illuminated surface of IC 63 using Spitzer archival data of molecular hydrogen. They used the short and long wavelength (SL, 5.214.5 μm; LL, 14.038.0 μm) low resolution modules ($R \sim 60$–130). The spatial coverage of the SL mode was ≈0.8 × 1.0 arcmin^2 (i.e., 0.046 × 0.058 pc^2 at the distance of IC 63) and the spatial coverage of the LL mode on the tip of the IC 63 nebula was ≈2.8 × 2.4 arcmin^2 (i.e., 0.16 × 0.14 pc^2).

They found the cooler temperature ($T = 207 \pm 30$ K) to be associated with a higher column density of 2.3×10^{20} cm^{-2} and the warmer component ($T = 740 \pm 47$ K) to be associated with a lower density 9.7×10^{17} cm^{-2} region. Their values are in good agreement with the hot component (i.e., $T = 685 \pm 68$ K) of Thi et al. (2009). But these values are higher than what we found as a hot component (i.e., $T_{\rm ridge} = 562^{+52}_{-43}$ K) with SOFIA/EXES higher spatial resolution observations. This suggests that Thi et al. (2009) and Andrews et al. (2018) get an averaged value of temperature in the bigger aperture of the ISO/SWS and Spitzer/IRS, respectively. Whereas EXES observations are further capable of resolving temperature of PDRs.

Soam et al. (2021) showed that the collisional disalignment rate of the dust grains causing the observed polarization follow a bifurcated relation with respect to the gas density. The two observed sequences in derived disalignment rate correspond to lines of sight in front and behind gas clumps, as seen in the $HCO^+(J = 1-0)$ map of the cloud. A two-temperature structure in the gas, caused by variable internal shading by molecular clumps, would explain this observed bifurcation.

We used PDR modeling in Section 3.2 to estimate the density of the gas adapting the radiative transfer equation and assuming that the heating is due to the photoelectric effect. The density of gas is found to be 5×10^3 cm^{-3}. Our estimation of density is consistent with the value reported by Jansen et al. (1994). Habart et al. (2011) in their investigation on number of PDRs stated that for the physical conditions prevailing in our

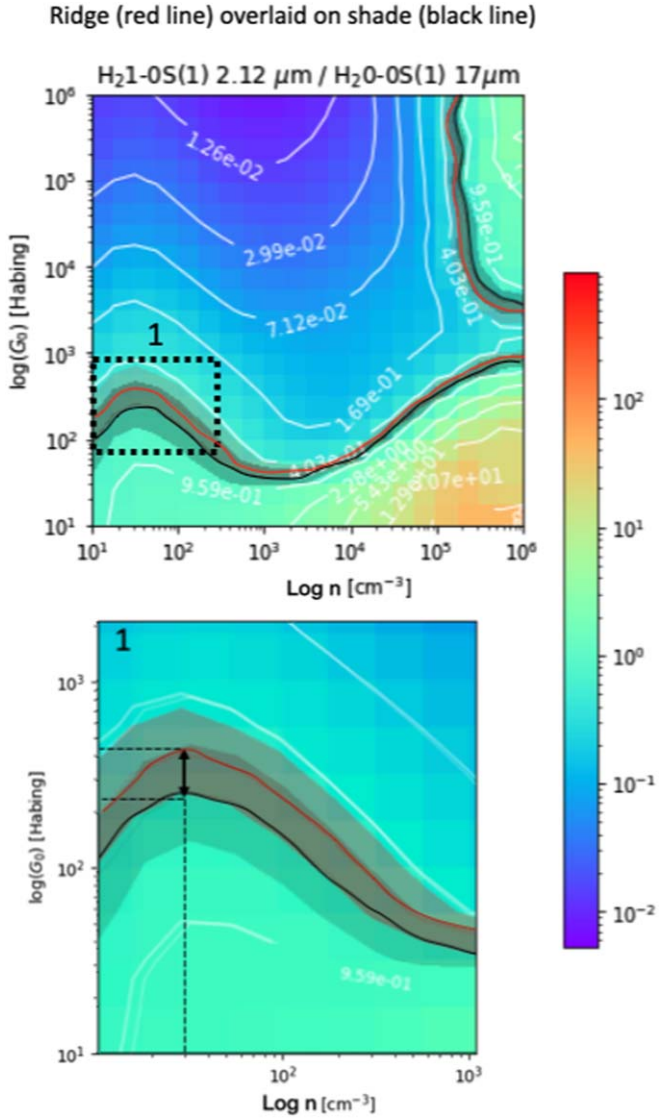

Figure 4. Upper panel shows the contour plot of H_2 1−0 S(1)/0−0 S(1) line ratios in the ridge (red line) and shady (black line) regions as functions of density and UV intensity G_0 with respect to the Habing field, adapted from Kaufman et al. (2006). The width of the shade represents 3σ confidence. Dashed box 1 shown in the in the upper panel is zoomed-in in the lower panel.

PDRs, the heating is mainly due to the photoelectric effect. Authors also report that for a range of H_2 formation rates and densities in various PDRs, the gas temperature versus PDR depth profile remains insensitive to the fraction of molecular hydrogen. However, a higher formation rate of molecular hydrogen may shift the photodissociation front toward higher temperatures.

The nondetection of H_2 pure rotational emission in the sunny part of the nebula is, in retrospect, not surprising. The locations of the sunny and shady regions were chosen based on mid/far-infrared continuum and H_2 $v = 1-0$ S(1) line imaging. To allow for the presence of H_2 not detected by the fluorescent emission—possibly as a result of a highly clumpy medium on small scales—(sunny) locations star-ward of the fluorescent ridge were included in our observations. However, given the sharp transition expected from atomic to molecular forms of hydrogen, caused by the self-shielding of the molecule (e.g., Federman et al. 1979) the nondetection of H_2 in the sunny regions is consistent with this sharp transition and indicates that the PDR is not very clumpy.

5. Conclusions

We have reinvestigated the temperature in the IC 63 PDR using pure rotational molecular hydrogen observations of S(1) and S(5) lines using SOFIA/EXES observations. A similar investigation was done by Thi et al. (2009) in this nebulae using lower spatial resolution ISO/SWS observations. The higher spatial resolution of EXES over SWS enables us to spatially resolve temperature in this PDR. Thi et al. (2009) reported two components of gas using S(0), S(1), S(3), and S(5) pure rotational lines of molecular hydrogen. The warm component is found to be at $T_{ex} = 106 \pm 11$ K and the hot gas component is seen at $T_{ex} = 685 \pm 68$ K. We divided IC 63 PDR into shady, ridge, and sunny sides for our investigation. By constructing a rotation diagram using S(1) and S(5) line data from EXES, we obtained a temperature of $T_{ex} = 562^{+52}_{-43}$ K toward the ridge and $T_{ex} = 495^{+28}_{-25}$ K in the shady side. The PDR toolbox code was used to model the line ratios of detected emission in H_2 1−0 S(1) and 0−0 S(1) transitions. Our model suggests a lower value of FUV radiation (G_0) in the shade as compared to the one in the ridge. We used this damping in FUV radiation to estimate the optical depth of the PDR. Our results emphasize that SOFIA/EXES has the capability to resolve and provide detailed information on gas temperature and density of such regions. We are attempting to expand this work through observations of the S(2) and S(4) transitions from IC 63.

We thank the anonymous referee for helping us to improve the content of the paper considerably. Authors also thank the EXES/SOFIA team for the data. SOFIA is jointly operated by the Universities Space Research Association, Inc. (USRA), under NASA contract NNA17BF53C, and the Deutsches SOFIA Institut (DSI) under DLR contract 50 OK 0901 to the University of Stuttgart. EXES is supported by NASA agreement 80NSSC19K1701. Financial support for the work in this paper was provided by NASA through award 07_0040 issued by USRA, and by the NSF through grant-1715876. J.K. acknowledges funding from the Moses Holden Scholarship in support of his PhD. A.S. thanks Mark Wolfire and Marc Pound for adding the required line ratio to their PDR toolbox. We thank Doug Hoffman (USRA/NASA Ames) for helping in calibration of the data. Financial support for the working this paper was provided by NASA through awards 07_0040 and 08_0067.

Facilities: EXES/SOFIA, CFHT.

Software: Astropy (Astropy Collaboration et al. 2013), Matplotlib (Hunter 2007), SciPy (Virtanen et al. 2020), NumPy (Harris et al. 2020).

ORCID iDs

Archana Soam https://orcid.org/0000-0002-6386-2906
B-G Andersson https://orcid.org/0000-0001-6717-0686
Janik Karoly https://orcid.org/0000-0001-5996-3600
Curtis DeWitt https://orcid.org/0000-0002-6528-3836
Matthew Richter https://orcid.org/0000-0002-8594-2122

References

Allers, K. N., Jaffe, D. T., Lacy, J. H., Draine, B. T., & Richter, M. J. 2005, ApJ, 630, 368
Andersson, B. G., Piirola, V., De Buizer, J., et al. 2013, ApJ, 775, 84
Andrews, H., Peeters, E., Tielens, A. G. G. M., & Okada, Y. 2018, A&A, 619, A170
Astropy Collaboration, Robitaille, T. P., Tollerud, E. J., et al. 2013, A&A, 558, A33
Bakes, E. L. O., & Tielens, A. G. G. M. 1994, ApJ, 427, 822
Bertoldi, F. 1997, in ESA Special Publication, Vol. 419, The First ISO Workshop on Analytical Spectroscopy, ed. A. M. Heras et al. (Noordwijk: ESA Publications), 67
Bohlin, R. C., Savage, B. D., & Drake, J. F. 1978, ApJ, 224, 132
Clarke, M., Vacca, W. D., & Shuping, R. Y. 2015, in ASP Conf. Ser., 495, Astronomical Data Analysis Software an Systems XXIV (ADASS XXIV), ed. A. R. Taylor & E. Rosolowsky (San Francisco, CA: ASP), 355
Draine, B. T., & Bertoldi, F. 1999, in ESA Special Publication, Vol. 427, The Universe as Seen by ISO (Noordwijk: ESA Publications)
Ehrenfreund, P., Krafft, C., Kochan, H., & Pirronello, V. 1998, Laboratory Astrophysics and Space Research, Vol. 236 (Dordrecht: Kluwer Academic)
Federman, S. R., Glassgold, A. E., & Kwan, J. 1979, ApJ, 227, 466
Gordon, I. E., Rothman, L. S., Tan, Y., Kochanov, R. V., & Hill, C. 2017, in 72nd Int. Symp. on Molecular Spectroscopy (Champaign, IL: Univ. Illinois), TJ08
Habart, E., Abergel, A., Boulanger, F., et al. 2011, A&A, 527, A122
Habart, E., Boulanger, F., Verstraete, L., Walmsley, C. M., & Pineau des Forêts, G. 2004, A&A, 414, 531
Habart, E., Walmsley, M., Verstraete, L., et al. 2005, SSRv, 119, 71
Harris, C. R., Millman, K. J., van der Walt, S. J., et al. 2020, Natur, 585, 357
Hunter, J. D. 2007, CSE, 9, 90
Jansen, D. J., van Dishoeck, E. F., & Black, J. H. 1994, A&A, 282, 605
Jura, M. 1975, ApJ, 197, 581
Karr, J. L., Noriega-Crespo, A., & Martin, P. G. 2005, AJ, 129, 954
Kaufman, M. J., Wolfire, M. G., & Hollenbach, D. J. 2006, ApJ, 644, 283
Lambert, D. L., & Danks, A. C. 1986, ApJ, 303, 401
McKee, C. F., & Ostriker, J. P. 1977, ApJ, 218, 148
Millar, T. J., Bennett, A., Rawlings, J. M. C., Brown, P. D., & Charnley, S. B. 1991, A&AS, 87, 585
Nadeau, D., Riopel, M., & Geballe, T. R. 1991, ApJL, 372, L103
Pound, M. W., & Wolfire, M. G. 2008, in ASP Conf. Ser., 394, Astronomical Data Analysis Software and Systems XVII, ed. R. W. Argyle, P. S. Bunclark, & J. R. Lewis (San Francisco, CA: ASP), 654
Puget, P., Stadler, E., Doyon, R., et al. 2004, Proc. SPIE, 5492, 978
Richter, M. J., Dewitt, C. N., McKelvey, M., et al. 2018, JAI, 7, 1840013
Röllig, M., Abel, N. P., Bell, T., et al. 2007, A&A, 467, 187
Rosenthal, D., Bertoldi, F., & Drapatz, S. 2000, A&A, 356, 705
Skrutskie, M. F., Cutri, R. M., Stiening, R., et al. 2006, AJ, 131, 1163
Soam, A., Andersson, B. G., Acosta-Pulido, J., et al. 2021, ApJ, 907, 93
Sternberg, A., & Dalgarno, A. 1989, ApJ, 338, 197
Temi, P., Hoffman, D., Ennico, K., & Le, J. 2018, JAI, 7, 1840011
Thi, W. F., van Dishoeck, E. F., Bell, T., Viti, S., & Black, J. 2009, MNRAS, 400, 622
Timmermann, R., Bertoldi, F., Wright, C. M., et al. 1996, A&A, 315, L281
van Dishoeck, E. F. 2004, ARA&A, 42, 119
Virtanen, P., Gommers, R., Oliphant, T. E., et al. 2020, NatMe, 17, 261
Weingartner, J. C., & Draine, B. T. 1999, AAS Meeting Abstracts, 195, 74.04
Weingartner, J. C., & Draine, B. T. 2001, ApJS, 134, 263
Weingartner, J. C., Draine, B. T., & Barr, D. K. 2006, ApJ, 645, 1188
Weingartner, J. C., & Jordan, M. E. 2008, ApJ, 672, 382
Whittet, D. C. B. 2003, Dust in the Galactic Environment (Bristol: IOP)
Wolfire, M. G., & Kaufman, M. J. 2011, in Photodissociation Regions, ed. M. Gargaud et al. (Berlin: Springer), 1236
Wolniewicz, L., Simbotin, I., & Dalgarno, A. 1998, ApJS, 115, 293